

## Ruby NMR laser: A phenomenon of spontaneous self-organization of a nuclear spin system

P. Bösiger, E. Brun, and D. Meier

*Physik-Institut, Universität Zürich, Zürich, Switzerland*

(Received 16 January 1978)

Radio wave amplification by stimulated emission of radiation (NMR laser) was observed in  $\text{Al}_2\text{O}_3:\text{Cr}^{3+}$  (ruby) with the  $^{27}\text{Al}$  spin system pumped to an inverted Zeeman state by means of dynamic nuclear polarization (DNP) and with an LC circuit tuned to the NMR transitions. A theory is developed which combines standard Bloch equations with the dynamic equations of a heat-reservoir model for the spin dynamics. Experimental data concerning the relaxation and polarization mechanisms in the nonradiant state are presented, and the parameters of the reservoir model are determined. In accord with these results, dynamic NMR laser equations for different modes of operation (continuous or pulsed) are derived from which the threshold of the NMR laser, its critical behavior near threshold, and its transient response after Q-switch tuning can be calculated. The agreement between theory and experiments in the superradiant state reflects unambiguously the interplay between nuclear-spin relaxation, DNP, spin fluctuations, and the self-induced ordering of the  $^{27}\text{Al}$  spins perpendicular to the applied field. In particular, the results highlight the decisive role of the electronic dipole-dipole system in the spin and NMR laser dynamics of ruby. Special emphasis is placed on the close relationship between the NMR laser, as a system far from thermal equilibrium which shows the phenomenon of cooperative self-organization, and a system at thermal equilibrium which undergoes a second-order phase transition. Thus, the rotating nuclear-spin magnetization is treated as an order parameter.

### I. INTRODUCTION

Recently,<sup>1,2</sup> we reported the discovery of a self-induced coherent rf oscillation of the  $^{27}\text{Al}$  nuclear-spin system in  $\text{Al}_2\text{O}_3:\text{Cr}^{3+}$  at the temperature of liquid helium. These oscillations can be observed in a strong, static magnetic field, when the coil of a LC circuit is tuned to one of the  $^{27}\text{Al}$  NMR frequencies while powerful microwave radiation is supplied to the sample in the vicinity of a properly selected  $\text{Cr}^{3+}$  ESR line. By means of dynamic nuclear polarization (DNP), the microwave source acts as a pump causing the population inversion of the nuclear Zeeman states. The nuclear-spin system is brought to a negative spin temperature and a negative, longitudinal magnetization  $M_z$  is thus formed. The coil provides the self-induced radiation field  $B_1^{\text{ind}}$  necessary to cause phase-locked spin flips. This field then is responsible for the coherent slaving of the individual members of the  $^{27}\text{Al}$  spin ensemble in the superradiant state in which a transverse, rotating component  $M_y$  of the nuclear magnetization is present. Since the combined system has properties typical of a laser (or maser), it may be called NMR laser.

The ruby NMR laser can be operated in either the continuous wave (cw) mode or in the pulsed (p) mode. Both require a spin inversion which is above a critical threshold. In the p mode, using a Q-switch technique, transients are found which start with a strong superradiant burst and evolve

into a relaxation oscillation. With the pump off, the signal decays to zero; with the pump on, the cw state is reached.

In our Letter<sup>1</sup> we showed that the first superradiant pulse after the Q-switch procedure can quantitatively be explained by a Bloch-type equation for a radiant two-state system. The nonlinear equations of motion for  $M_x$  and  $M_y$  contain driving terms proportional to the slaving field  $B_1^{\text{ind}}$ . The dephasing of the transverse magnetization is accounted for by a term proportional to the cw NMR linewidth, or to  $1/T_2$ . These equations are adequate to calculate the short-time behavior (typically of the order of msec) if a small initial value of  $M_y$  is assumed. However, they cover neither the full range of the transients (lasting one second, typically) nor the final cw NMR laser state. Furthermore, they do not take into account the fluctuations which are responsible for the ignition of the NMR action.

In order to describe the NMR laser more completely, the quoted Bloch equations have to be generalized. Since the transition from the pumped, but incoherent state into the superradiant state, as well as the level of the cw oscillations depend in a rather complex way on the spin dynamics of  $\text{Al}_2\text{O}_3:\text{Cr}^{3+}$ , terms have to be added which represent (a) the spin-lattice relaxation, (b) the spin-spin interaction between the relevant spin subsystems, (c) the microwave pump, and (d) the fluctuations. To derive explicit expressions for

(a), (b), and (c), a systematic treatment of the DNP and relaxation mechanism is required.

In this paper, which is an amplification and extension of our earlier Letter, we describe, in Sec. II, various experiments with regard to the dynamics of the different spin systems in ruby. We present a selection of experimental results and their quantitative explanation which we consider as essential for the understanding of the NMR laser dynamics. In particular we discuss a thermodynamic approach, based on the concept of spin temperature, in order to explain the polarization and depolarization properties. A heat-reservoir model is introduced, and a set of simultaneous differential equations is presented which are in good agreement with a large body of experimental facts.

In Sec. III we proceed to generalize the Bloch equations given in our Letter. We incorporate the results of Sec. II by means of the explicit expressions for (a), (b), and (c). Furthermore, we relate the fluctuation term ( $d$ ) to the Nyquist noise of the coil, which can be calculated. We then present numerical solutions of the obtained NMR laser equations which can be compared with experimental radiation patterns.

A discussion is included which illustrates the close relationship of the spontaneous superradiant transition with a phase transition from a disordered to an ordered state. Although being far from thermal equilibrium, certain aspects of the superradiant transition are in common with second-order phase transitions of equilibrium systems, e.g., superconductors, ferromagnets, etc. Hence, we derive a dynamic equation for the order parameter, here the transverse magnetization  $M_v$ , which holds near the critical point of the NMR laser. From this equation (being the subject also of the Landau-Hopf theory of bifurcation,<sup>3,4</sup> as well as of the interdisciplinary field of synergetics which was mainly put forward by Haken<sup>5</sup>) we obtain the explicit threshold condition and the power law for the NMR laser output near threshold.

Viewed from these perspectives, the ruby NMR laser is an instructive example for a many-body system showing the phenomenon of spontaneous, cooperative self-organization. Its dynamics are of broad interest since the problem of stability plays a central role in a great variety of fields such as engineering, meteorology, geophysics, fluid mechanics, biology, etc.<sup>6</sup> Thus, our detailed investigation reflects not only the underlying mechanisms of spin relaxation but provides general and quantitative information of the synergetic properties of coupled spins and their modes of excitations.

## II. DNP AND SPIN RELAXATION IN RUBY

### A. Heat-reservoir model

In solid insulators containing both electronic and nuclear spins, there can exist a thermal contact between the nuclear Zeeman and the electronic dipole-dipole system. The exchange of spin energy is possible if the nuclear Zeeman splitting is comparable to the width of the ESR lines. This thermal mixing is the physical background of the thermodynamic model of coupled heat reservoirs as proposed by Buishvili,<sup>7</sup> Kozhushner,<sup>8</sup> and Wenckebach,<sup>9</sup> and refined by many others.

In essence, the Hamiltonian is broken up in mutually commuting and noncommuting terms,  $\mathcal{H}_i$  and  $\mathcal{H}_{ki}$ , respectively. To each of the commuting operators, which represent subsystems with many degrees of freedom, a heat reservoir  $\{\mathcal{H}_i\}$  is assigned. A steady state of a reservoir is characterized by the spin temperature  $\theta_i$ , or better, by the inverse spin temperature  $\beta_i = 1/k_B\theta_i$ . The internal energy becomes  $E_i = c_i\beta_i$ , where  $c_i$  is the heat capacity. The noncommuting terms describe either internal couplings (spin-spin, spin-lattice) or interactions with external fields. They are treated as perturbations causing energy to flow to and from the heat reservoirs. The internal couplings tend to equalize the reservoir temperatures with characteristic time constants  $\tau_{ki}$ . The interactions with the external fields lead to a nonequilibrium state, for example, under DNP or partial saturation conditions. In this sense we speak of relaxation and pump terms, assuming both to be so small that each of the coupled reservoirs passes through quasiequilibrium states.

For ruby ( $\text{Al}_2\text{O}_3:\text{Cr}^{3+}$ ), Atsarkin *et al.*<sup>10</sup> demonstrated the important role of the electronic dipole-dipole system with regard to DNP and the spin-lattice relaxation of bulk  $^{27}\text{Al}$ . Later, Hundt and co-workers<sup>11, 12</sup> extended the investigation of the thermal contact to the  $^{17}\text{O}$  spins of natural abundance, and to those  $^{27}\text{Al}$  nuclei which are near neighbors of the magnetic  $\text{Cr}^{3+}$  ions (impurity-shifted  $^{27}\text{Al}^*$ , hereafter). In a series of rather qualitative experiments concerning the polarization, depolarization, and partial saturation properties of the nuclear-spin systems the authors showed that this contact causes an indirect coupling of the otherwise noninteracting Zeeman systems of  $^{27}\text{Al}$ ,  $^{27}\text{Al}^*$ , and  $^{17}\text{O}$ . This then led us to the hypothesis, that the nuclear Zeeman systems in ruby can be described thermodynamically also in situations where the overall equilibrium is not achieved. In fact, the results suggested that under stationary DNP conditions, in particular, a common nuclear-spin temperature is reached which is independent of the  $\text{Cr}^{3+}$  Zeeman order. Similar results have since

been reported for various other substances such as  $\text{TiO}_2:\text{Cr}^{3+}$ ,<sup>13,14</sup>  $\text{LiF}:\text{F-centers}$ ,<sup>15</sup> and propane-diol: $\text{Cr}^{3+}$ .<sup>16</sup>

In order to prove the hypothesis of the existence of a spin temperature in ruby, a systematic investigation of the spin dynamics was started. To analyze the experimental results, which will be presented in the forthcoming paragraphs, we introduce the three nuclear Zeeman reservoirs  $\{\mathcal{H}_{\text{Al}}\}$ ,  $\{\mathcal{H}_{\text{Al}^*}\}$ , and  $\{\mathcal{H}_{\text{O}}\}$  of the dense  $^{27}\text{Al}$ , the dilute, impurity-shifted  $^{27}\text{Al}^*$ , and of the dilute  $^{17}\text{O}$  spins, respectively. The  $^{53}\text{Cr}$  nuclear-spin system is not included here. These Zeeman systems interact predominantly with the electronic dipole-dipole reservoir  $\{\mathcal{H}_{\text{SS}}\}$  through magnetic dipole and hyperfine interactions. Finally, we have  $\{\mathcal{H}_{\text{S}}\}$  and  $\{\mathcal{H}_{\text{L}}\}$ , the electronic Zeeman reservoir and the lattice, respectively.

Since the spins interact not only magnetically but couple also to the electric crystal field, this then leads to the splitting of the pure Zeeman lines into multiplets, e.g., the five quadrupolar split lines of  $^{27}\text{Al}$  and  $^{17}\text{O}$ . Thus, if necessary, a subdivision of the spin systems in fictitious spin- $\frac{1}{2}$  two-state systems is possible to which separated heat reservoirs can be assigned.

In a simplified version of the reservoir model for ruby, where we assume thermal cooling as the cause of DNP and nuclear relaxation, we neglect the electric interactions for the time being. They can be incorporated later without difficulties. With the static Hamiltonian

$$\mathcal{H} = \mathcal{H}_{\text{S}} + \mathcal{H}_{\text{SS}} + \mathcal{H}_{\text{Al}} + \mathcal{H}_{\text{Al}^*} + \mathcal{H}_{\text{O}} + \mathcal{H}_{\text{L}}, \quad (2.1)$$

a quasistationary state of the heat reservoirs has the density matrix

$$\rho = (1/\Sigma) \exp(-\beta_{\text{S}}\mathcal{H}_{\text{S}} - \beta_{\text{SS}}\mathcal{H}_{\text{SS}} - \beta_{\text{Al}}\mathcal{H}_{\text{Al}} - \beta_{\text{Al}^*}\mathcal{H}_{\text{Al}^*} - \beta_{\text{O}}\mathcal{H}_{\text{O}} - \beta_{\text{L}}\mathcal{H}_{\text{L}}), \quad (2.2)$$

of which only the high temperature limit is used.

Starting from the overall equilibrium  $\beta_{\text{S}} = \beta_{\text{SS}} = \beta_{\text{Al}} = \beta_{\text{Al}^*} = \beta_{\text{O}} = \beta_{\text{L}}$ , strong microwave pumping power delivered to the sample near the center of the ESR line couples  $\{\mathcal{H}_{\text{S}}\}$  with  $\{\mathcal{H}_{\text{SS}}\}$  which, according to the Provotorov equations,<sup>17</sup> amounts to a cooling (or heating to negative temperatures!) of the  $\text{Cr}^{3+}$ - $\text{Cr}^{3+}$  interaction system. Relaxation processes involving two mutual spin flips combined with a simultaneous nuclear spin flip<sup>18</sup> cause a transfer of spin energy between the unbalanced reservoirs  $\{\mathcal{H}_{\text{SS}}\}$ ,  $\{\mathcal{H}_{\text{Al}}\}$ ,  $\{\mathcal{H}_{\text{Al}^*}\}$ , and  $\{\mathcal{H}_{\text{O}}\}$ . Hence the nuclear spins become dynamically polarized. The lattice, however, is assumed to remain at the temperature of the He bath.

For this simple model of DNP by thermal contact, the spin dynamics can be depicted by the en-

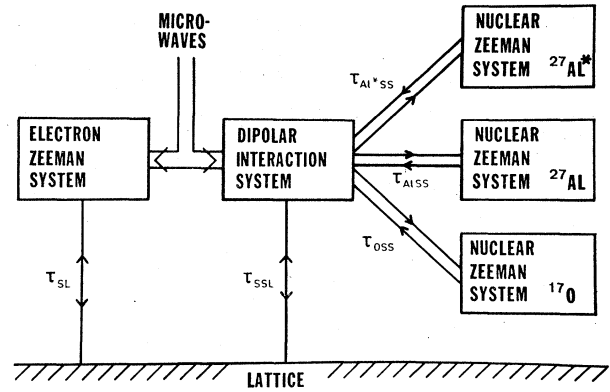


FIG. 1. Energy-flow diagram for the spin dynamics in ruby: $\text{Al}_2\text{O}_3:\text{Cr}^{3+}$ .

ergy-flow diagram of Fig. 1. The time evolution of the inverse reservoir temperatures follows from a set of simultaneous differential equations:

$$\begin{aligned} \frac{d\beta_{\text{Al}}}{dt} &= -\frac{1}{\tau_{\text{AlSS}}}(\beta_{\text{Al}} - \beta_{\text{SS}}), \\ \frac{d\beta_{\text{Al}^*}}{dt} &= -\frac{1}{\tau_{\text{Al}^*\text{SS}}}(\beta_{\text{Al}^*} - \beta_{\text{SS}}), \\ \frac{d\beta_{\text{O}}}{dt} &= -\frac{1}{\tau_{\text{OSS}}}(\beta_{\text{O}} - \beta_{\text{SS}}), \\ \frac{d\beta_{\text{SS}}}{dt} &= -\frac{c_{\text{Al}}}{c_{\text{SS}}} \frac{1}{\tau_{\text{AlSS}}}(\beta_{\text{SS}} - \beta_{\text{Al}}) - \frac{c_{\text{Al}^*}}{c_{\text{SS}}} \frac{1}{\tau_{\text{Al}^*\text{SS}}}(\beta_{\text{SS}} - \beta_{\text{Al}^*}) \\ &\quad - \frac{c_{\text{O}}}{c_{\text{SS}}} \frac{1}{\tau_{\text{OSS}}}(\beta_{\text{SS}} - \beta_{\text{O}}) - \frac{1}{\tau_{\text{SSL}}}(\beta_{\text{SS}} - \beta_{\text{L}}) \\ &\quad + \pi(\gamma_{\text{S}} B_1^{\text{MW}})^2 g(\omega_{\text{S}} - \omega_{\text{m}}) \frac{\omega_{\text{S}} - \omega_{\text{m}}}{\delta \omega^2} \\ &\quad \times [\omega_{\text{S}} \beta_{\text{S}} - (\omega_{\text{S}} - \omega_{\text{m}}) \beta_{\text{SS}}], \\ \frac{d\beta_{\text{S}}}{dt} &= -\frac{1}{\tau_{\text{SL}}}(\beta_{\text{S}} - \beta_{\text{L}}) \\ &\quad + \pi(\gamma_{\text{S}} B_1^{\text{MW}})^2 g(\omega_{\text{S}} - \omega_{\text{m}}) \left( \frac{\omega_{\text{S}} - \omega_{\text{m}}}{\omega_{\text{S}}} \beta_{\text{SS}} - \beta_{\text{S}} \right). \end{aligned} \quad (2.3)$$

Here  $g(\omega)$  and  $\delta\omega$  are shape and width of the ESR line while  $\omega_{\text{m}}$  represents the frequency of the microwave field.

If the nuclear spins are probed with a weak rf field, NMR signals result which are directly related to the respective inverse nuclear-spin temperature. Hence, standard NMR techniques can be applied to spin-dynamic experiments.

#### B. Experimental details

To test the proposed heat-reservoir model of DNP, we determined the time evolution of  $\beta_{\text{Al}}$ ,

$\beta_{Al}^*$ , and  $\beta_O$  either with the microwave pump on (polarization) or off (depolarization), after preparing the system in a well-defined initial state. For this, we monitored the NMR signal of a  $Q$ -meter detector driven by a Hewlett-Packard 8660B frequency synthesizer. The signals with frequencies near 12 MHz were stored in a Nicolet-1020 A signal averager. Spin saturation was avoided, or, if it occurred, corrected in order to keep the signal intensity proportional to the corresponding inverse nuclear-spin temperature. The experimental data points were then fitted with appropriate solutions of Eq. (2.3) and a consistent set of constants was determined.

The results to be presented refer to two ruby specimens with a volume of about  $1 \text{ cm}^3$  and  $10^{-2} \text{ cm}^3$ , respectively. Both were cut from the same single crystal with a  $\text{Cr}^{3+}$  concentration of nominally 0.02%. For bulk  $^{27}\text{Al}$  we used the small specimen with a filling factor of less than 0.1, therefore avoiding nonlinearities in the tank circuit.<sup>19</sup> For dilute  $^{27}\text{Al}^*$  and  $^{17}\text{O}$ , however, the large specimen with a filling factor of about 0.6 was required in order to obtain an acceptable signal-to-noise ratio.

The microwave power ( $\sim 100 \text{ mW}$ ) stemmed from an OKI-30V12 klystron which was operated at 30.6 GHz, typically. The microwaves were guided through a precision attenuator and a microwave switch to a  $13 \times 13 \times 50$ -mm multimode brass cavity with a  $Q$  of about  $10^3$ . The cavity was matched to the stainless steel waveguides by a simple, rectangular iris of  $6.3 \times 0.5 \text{ mm}$ . It contained the NMR pick-up coil with the ruby sample. The axis of the coil was made parallel to the long side of the cavity. Neither the exact size nor the positioning were critical for the experiments.

The measurements were performed in a static field of about 1.1 T and in the temperature range from 1.6 to 4.2 K. A timing unit controlling the microwave switch, the NMR frequency sweep, and the signal-averaging system made an automatic accumulation of experimental data possible.

### C. Experimental results and analysis

#### 1. Bulk $^{27}\text{Al}$

A number of polarization and depolarization curves were determined for different values of the  $\text{Cr}^{3+}$  content, the magnetic field  $B_0$ , the lattice temperature  $\theta_L$ , and the angle  $\vartheta$  between the crystal  $c$  axis and the field direction. Since the heat capacity of the dense  $\{\mathcal{H}_{Al}\}$  is many orders of magnitude larger than those of the dilute  $\{\mathcal{H}_O\}$  and  $\{\mathcal{H}_{Al}^*\}$ , these two reservoirs can be discarded in the analysis of the  $^{27}\text{Al}$  data. Thus, the spin dynamics is governed by the reduced set of differ-

ential equations:

$$\begin{aligned} \frac{d\beta_{Al}}{dt} &= -\frac{1}{\tau_{AlSS}} (\beta_{Al} - \beta_{SS}), \\ \frac{d\beta_{SS}}{dt} &= -\frac{c_{Al}}{c_{SS}} \frac{1}{\tau_{AlSS}} (\beta_{SS} - \beta_{Al}) - \frac{1}{\tau_{SSL}} (\beta_{SS} - \beta_L) \\ &\quad + \pi(\gamma_S B_1^{MW})^2 g(\omega_S - \omega_m) \frac{\omega_S - \omega_m}{\delta \omega^2} \\ &\quad \times [\omega_S \beta_S - (\omega_S - \omega_m) \beta_{SS}], \\ \frac{d\beta_S}{dt} &= -\frac{1}{\tau_{SL}} (\beta_S - \beta_L) \\ &\quad + \pi(\gamma_S B_1^{MW})^2 g(\omega_S - \omega_m) \left( \frac{\omega_S - \omega_m}{\omega_S} \beta_{SS} - \beta_S \right). \end{aligned} \quad (2.4)$$

Since the solution depends strongly on the heat capacities  $c_S$  and  $c_{SS}$ , the equations can be simplified further by setting  $\beta_S = \beta_L = \text{const.}$  With the initial conditions  $\beta_{Al}(0) = \beta_{Al}^0$  and  $\beta_{SS}(0) = \beta_{SS}^0$ , we find

$$\beta_{Al} = A_1 e^{\lambda_1 t} + A_2 e^{\lambda_2 t} + \frac{\bar{g}}{f - a\kappa} \beta_L, \quad (2.5)$$

$$\beta_{SS} = \frac{\lambda_1 + a}{a} A_1 e^{\lambda_1 t} + \frac{\lambda_2 + a}{a} A_2 e^{\lambda_2 t} + \frac{\bar{g}}{f - a\kappa} \beta_L,$$

with

$$\begin{aligned} \kappa &= c_{Al}/c_{SS}, \quad a = 1/\tau_{AlSS}, \quad b = 1/\tau_{SSL}, \\ \lambda_1 &= \frac{1}{2} \left\{ -(a+f) + [a^2(1+4\kappa) - 2af + f^2]^{1/2} \right\}, \\ \lambda_2 &= \frac{1}{2} \left\{ -(a+f) - [a^2(1+4\kappa) - 2af + f^2]^{1/2} \right\}, \\ A_1 &= \frac{(\beta_{Al}^0 - k)(\lambda_2 + a) + a(\beta_{SS}^0 - k)}{\lambda_2 - \lambda_1}, \end{aligned}$$

$$c = \pi(\gamma_S B_1^{MW})^2 g(\omega_S - \omega_m)(\omega_S - \omega_m)/\delta \omega^2,$$

$$f = a\kappa + b + c(\omega_S - \omega_m), \quad \bar{g} = b + c\omega_S, \quad k = \bar{g}/(f - a\kappa)\beta_L.$$

First, we consider the depolarization. The sample is dynamically polarized and then, at  $t=0$ , the microwaves are turned off. For  $B_1^{MW}=0$ , we have  $\lambda_1 < \lambda_2$ . The exponential term with  $\lambda_2$  describes the fast approach to the thermal equilibrium of  $\{\mathcal{H}_{SS}\}$  and  $\{\mathcal{H}_{Al}\}$ . Since  $\{\mathcal{H}_{SS}\}$  and  $\{\mathcal{H}_{Al}\}$  are practically always at the same temperature, a single exponential decay of the NMR signal with the time constant  $1/\lambda_1$  is anticipated. The experimental depolarization time  $\tau_{\text{depAl}} = 1/\lambda_1$  is related to the coupling constants by

$$\tau_{AlSS} = \tau_{\text{depAl}} \left( 1 + \frac{\kappa \tau_{SSL}}{\tau_{SSL} - \tau_{\text{depAl}}} \right). \quad (2.6)$$

Thus, by fitting a single exponential to the experimental data points, possible pairs of  $\tau_{AlSS}$  and  $\tau_{SSL}$  can be determined. The absolute values of

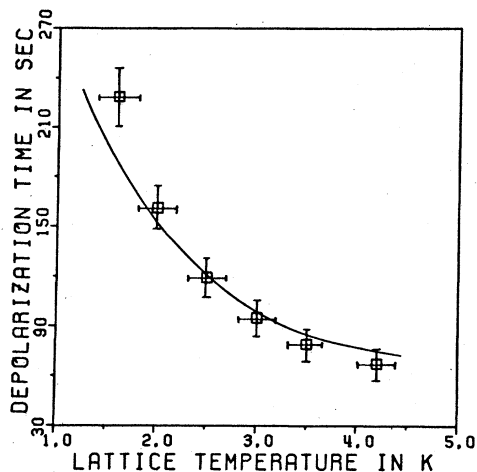


FIG. 2. Temperature dependence of the depolarization time of  $^{27}\text{Al}$  for  $B_0=1.1$  T and  $\vartheta=0^\circ$ .

these two coupling constants, however, are obtained from a fit of the temperature-dependent depolarization time of Fig. 2, and the assumption of equal temperature dependence of  $\tau_{SSL}$  and of  $\tau_{SL}$  [ $1/\tau_{SL} \sim \coth(\hbar\omega_S/k_B\theta_L)$ ] together with a temperature-independent value of  $\tau_{AlSS}$ . For a sample with parameters as listed in Table I, the result is depicted in Fig. 3.

Next, we treat the polarization of  $^{27}\text{Al}$ . The shape function of the ESR line and the magnitude of the polarizing microwave field have to be assumed. If we approximate the ESR line with a Gaussian and choose the reasonable value  $B_1^{MW} = 2.5 \times 10^{-3}$  G, the nuclear polarization curve can then be fitted using the same coupling constants

TABLE I. Numerical values for the parameters of our specific sample.

	$B_0=0.675$ T	$B_0=1.095$ T
$N_{\text{Al}}$ ( $\text{cm}^{-3}$ )		$4.4 \times 10^{22}$
$N_{\text{Cr}}$ ( $\text{cm}^{-3}$ )		$8.6 \times 10^{18}$
$\delta\omega$ ( $\text{sec}^{-1}$ )		$0.58 \times 10^9$
$c_{\text{Al}}$ ( $\text{sec}^{-2} \text{cm}^{-3}$ )	$0.28 \times 10^{39}$	$0.75 \times 10^{39}$
$c_{\text{SS}}$ ( $\text{sec}^{-2} \text{cm}^{-3}$ )	$0.36 \times 10^{37}$	$0.36 \times 10^{37}$
$\kappa$	78	206

as for the depolarization curve above. The fit is shown in Fig. 4.

These consistent results are an indirect proof of the heat-reservoir model, in particular of the existence of the electric dipole-dipole reservoir. The direct and final confirmation, however, will be obtained from the NMR laser dynamics of Sec. III.

Further, we found that the experimental coupling constants are nearly independent of the orientation of the crystal with respect to the magnetic field, except for conditions where two ESR lines overlap. In such regions cross relaxation<sup>10</sup> comes into play which, as an additional relaxation process, strongly affects the time constants. For  $\vartheta=0^\circ$ , the obtained values are in good agreement with predictions<sup>20, 21</sup> based on microscopic relaxation theories which include spin diffusion up to a distance of a few Å to the paramagnetic  $\text{Cr}^{3+}$  center.

The solutions of Eqs. (2.4) indicate further that the temperature of the electronic dipole-dipole system remains close to the temperature of the  $^{27}\text{Al}$  Zeeman system in either sort of experiments.

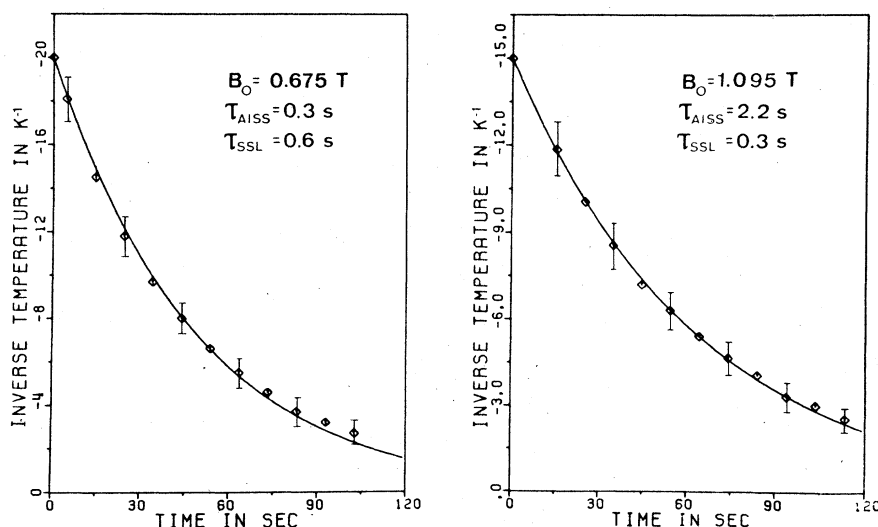


FIG. 3. Measured and fitted depolarization curves of  $^{27}\text{Al}$  for two different magnetic field strengths,  $\theta_L=4.2$  K and  $\vartheta=0^\circ$ .

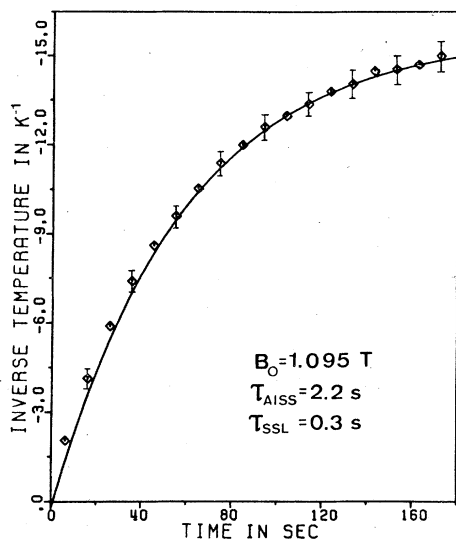


FIG. 4. Measured and fitted polarization curve of  $^{27}\text{Al}$  for  $\theta_L = 4.2$  K and  $\vartheta = 0^\circ$ .

This fact, which is a consequence of the condition  $c_{SS} \ll c_{Al}$ , will be a decisive factor in the dynamics of  $^{27}\text{Al}^*$  and  $^{17}\text{O}$ .

### 2. Impurity shifted $^{27}\text{Al}^*$

Some of the NMR properties of those  $^{27}\text{Al}$  nuclei which are near neighbors of the  $\text{Cr}^{3+}$  ions were reported in some earlier communications. Whereas Laurance *et al.*<sup>22</sup> observed the resonances directly by means of ENDOR, but only for the crystal  $c$  axis approximately parallel to the magnetic field, Hundt and co-workers<sup>11, 12</sup> detected over 200 of the impurity shifted lines using cw NMR for samples which were polarized by DNP. In contrast to ENDOR, the direct method works over the full angular range.

We measured the polarization and depolarization curves for a selected number of  $^{27}\text{Al}^*$  lines with highly improved accuracy. We found that they are identical to those of the bulk  $^{27}\text{Al}$  for all chosen orientations. The results indicate that the  $\{\mathcal{H}_{Al}^*\}$  also relaxes via  $\{\mathcal{H}_{SS}\}$  to the lattice and not by direct  $\text{Cr}^{3+}$  spin flips. A striking phenomenon is the fast increase of the NMR signals for some lines just after switching off the polarizing microwave field. This effect, as illustrated in Fig. 5, is most likely due to the partial saturation of  $\{\mathcal{H}_S\}$  by the microwaves and the fast recovery in the time  $\tau_{SL}$ , after they are turned off. It stems from a reordering of the electronic Zeeman system, as was observed also in ENDOR experiments.

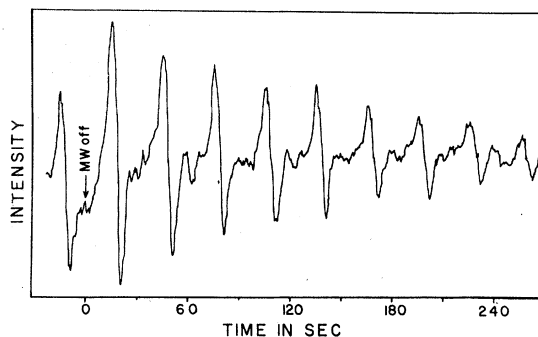


FIG. 5. Fast increase and decay of an NMR signal of  $^{27}\text{Al}^*$  after switching off the polarizing microwave field for  $B_0 = 1.095$  T,  $\theta_L = 1.6$  K, and  $\vartheta = 0^\circ$ .

### 3. Natural $^{17}\text{O}$

The dilute  $^{17}\text{O}$  spins, with an isotopic abundance of only 0.037%, differ in two important respects from bulk  $^{27}\text{Al}$  and impurity-shifted  $^{27}\text{Al}^*$ . The average dipole coupling to the  $\text{Cr}^{3+}$  ions is weak and spin diffusion among  $^{17}\text{O}$  spins is absent. It is therefore an astounding experimental fact that the  $^{17}\text{O}$  system can approach states which are characterized by a spin temperature, even under stationary DNP conditions. This again indicates that the thermal coupling to  $\{\mathcal{H}_{SS}\}$  influences strongly (although not completely) the polarization and relaxation properties of  $\{\mathcal{H}_O\}$ . To describe them quantitatively, a modified heat-reservoir model is introduced. Because of the large heat capacity of  $\{\mathcal{H}_{Al}\}$  ( $c_{Al} \gg c_{SS}, c_O$ ) and the strong coupling of  $\{\mathcal{H}_{Al}\}$  with  $\{\mathcal{H}_{SS}\}$  ( $\beta_{SS} \approx \beta_{Al}$ ), these two reservoirs are combined into an extended interaction system as indicated in Fig. 6. The evolution of  $\beta_O$  is determined by the single equation

$$\frac{d\beta_O}{dt} = -\frac{1}{\tau_{OSS}} (\beta_O - \beta_{SS}), \quad (2.7)$$

since the influence of  $\{\mathcal{H}_O\}$  on  $\{\mathcal{H}_{SS}\}$  is negligible.

Experimentally we observed that  $\tau_{OSS}$  is different for polarization and depolarization experiments. Therefore we introduce two time constants:  $\tau_{OSS}^{\text{MW}}$  when the microwaves are on, and  $\tau_{OSS}^0$  when they are off. This difference reflects the fact that the solid effect competes with dynamic cooling as a DNP mechanism.

In order to reach the highest possible polarization and a good signal-to-noise ratio for these extremely weak resonances, the measurements were performed at a crossing point of two ESR lines with

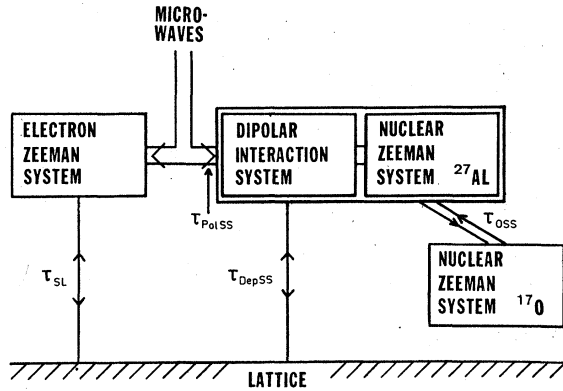


FIG. 6. Modified-heat-reservoir model for the description of the spin dynamics of  $^{17}\text{O}$ : The  $^{17}\text{O}$  system is coupled to an extended-interaction reservoir consisting of the electronic dipolar interaction and the nuclear  $^{27}\text{Al}$  Zeeman system.

$\vartheta = 60.4^\circ$ . For this orientation and with  $\theta_L = 1.6$  K, the polarization time of the interaction system is 60 sec, its depolarization time 240 sec.

In a first experiment, we started from a state of thermal equilibrium with the lattice ( $\beta_O = \beta_{SS} = \beta_L$ ). Thus, the polarization of  $\{\mathcal{H}_O\}$  is described by

$$\frac{d\beta_O}{dt} = -\frac{1}{\tau_{\text{Oss}}^{\text{MW}}} (\beta_O - \beta_{SS}), \quad (2.8a)$$

where the interaction system evolves according to

$$\beta_{SS} = (\beta_{SS}^\infty - \beta_L)(1 - e^{-t/\tau_{\text{polSS}}}) + \beta_L, \quad (2.8b)$$

$\beta_{SS}^\infty$  being the ultimately reached inverse spin temperature of the extended-interaction system under stationary DNP conditions. For  $\tau_{\text{Oss}}^{\text{MW}} \neq \tau_{\text{polSS}}$ , the solutions are

$$\begin{aligned} \beta_O &= A_3 e^{-t/\tau_{\text{Oss}}^{\text{MW}}} + A_4 e^{-t/\tau_{\text{polSS}}} + \beta_L, \\ \beta_{SS} &= (\beta_{SS}^\infty - \beta_L)(1 - e^{-t/\tau_{\text{polSS}}}) + \beta_L, \end{aligned} \quad (2.9)$$

with

$$A_3 = \beta_L - \beta_{SS}^\infty - A_4, \quad A_4 = \frac{\tau_{\text{polSS}}}{\tau_{\text{Oss}}^{\text{MW}} - \tau_{\text{polSS}}} \beta_{SS}^\infty.$$

For  $\tau_{\text{Oss}}^{\text{MW}} = \tau_{\text{polSS}}$ , in particular, we obtain a single exponential curve with the time constant  $\tau_{\text{polSS}}$ . In

Fig. 7 we show the best fit to the experimental data which yields  $\tau_{\text{Oss}}^{\text{MW}} = 30$  sec for our sample.

In a modified version of this experiment, we started from the polarized state. At  $t=0$ , we saturated  $\{\mathcal{H}_O\}$  with a short rf pulse and observed the subsequent repolarization of  $\{\mathcal{H}_O\}$  while keeping the microwaves on. Equation (2.8a) still holds with  $\beta_{SS} = \beta_{SS}^\infty$ . The best fit for our sample is obtained again with the same time constant  $\tau_{\text{Oss}}^{\text{MW}}$  as above. It is depicted in Fig. 8.

In a second experiment, we polarized  $\{\mathcal{H}_O\}$ , initially. At  $t=0$ , the microwaves were turned off, and we observed then the time evolution of  $\beta_O$ . The depolarization of  $\{\mathcal{H}_O\}$  is described by

$$\frac{d\beta_O}{dt} = -\frac{1}{\tau_{\text{Oss}}^0} (\beta_O - \beta_{SS}) \quad (2.10a)$$

and

$$\beta_{SS} = (\beta_{SS}^0 - \beta_L) e^{-t/\tau_{\text{depSS}}} + \beta_L. \quad (2.10b)$$

For  $\tau_{\text{Oss}}^0 \neq \tau_{\text{depSS}}$ , the solutions are

$$\begin{aligned} \beta_O &= A_3' e^{-t/\tau_{\text{Oss}}^0} + A_4' e^{-t/\tau_{\text{depSS}}} + \beta_L, \\ \beta_{SS} &= (\beta_{SS}^0 - \beta_L) e^{-t/\tau_{\text{depSS}}} + \beta_L, \end{aligned} \quad (2.11)$$

with

$$A_3' = \beta_O^0 - \beta_L - A_4', \quad A_4' = \frac{\tau_{\text{depSS}}}{\tau_{\text{depSS}} - \tau_{\text{Oss}}^0} (\beta_{SS}^0 - \beta_L).$$

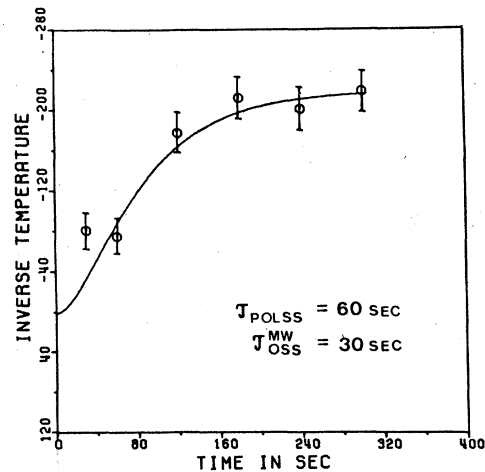


FIG. 7. Measured and fitted polarization curve of  $^{17}\text{O}$  for  $B_0 = 1.1$  T,  $\theta_L = 1.6$  K, and  $\vartheta = 60.4^\circ$ .

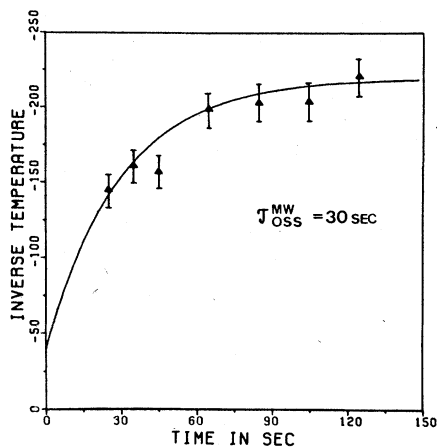


FIG. 8. Measured and fitted recovery curve of  $^{17}\text{O}$  after rf saturation for  $B_0=1.1$  T,  $\theta_L=1.6$  K, and  $\vartheta=60.4^\circ$ .

For  $\tau_{\text{OSS}}^0 = \tau_{\text{depSS}}$  we expect a single exponential depolarization curve with the time constant  $\tau_{\text{depSS}}$ . Figure 9 shows the best fit of (2.11) to the experimental results. The obtained time constant  $\tau_{\text{OSS}}^0 = 260$  sec is consistent with theoretical estimates.<sup>20, 21</sup>

In the last and crucial experiment we started from the polarized state again. At  $t=0$ , after turning off the microwaves, we saturated  $\{\mathcal{K}_O\}$  with a sharp rf pulse. We then observed the repolarization of  $\{\mathcal{K}_O\}$  followed by the depolarization. This observation proves unambiguously that the highly ordered compound interaction system indeed polarizes  $\{\mathcal{K}_O\}$  by thermal cooling and, hence, also governs the final relaxation towards the lattice temperature, as shown in Fig. 10. The ex-

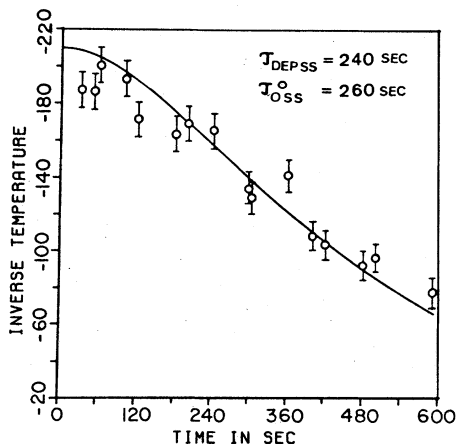


FIG. 9. Measured and fitted depolarization curve of  $^{17}\text{O}$  for  $B_0=1.1$  T,  $\theta_L=1.6$  K, and  $\vartheta=60.4^\circ$ .

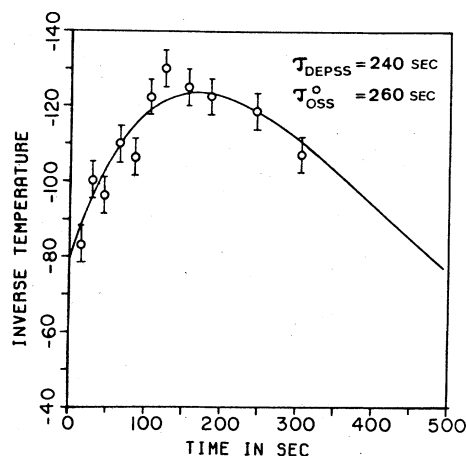


FIG. 10. Measured and fitted recovery and depolarization curve of  $^{17}\text{O}$  after switching off the microwave field and simultaneous rf saturation of the  $^{17}\text{O}$  system for  $B_0=1.1$  T,  $\theta_L=1.6$  K, and  $\vartheta=60.4^\circ$ .

perimental data can be fitted with the time constants found above.

#### 4. Nuclear-spin temperature

In the analysis of all the experiments discussed in this section, we supposed the existence of a thermodynamic equilibrium or quasiequilibrium within the nuclear-spin systems, each having a defined spin temperature. In a highly polarized Zeeman state, this temperature can be calculated from the relative intensities of the quadrupolar split NMR lines, if the population number obeys the Boltzmann law and if nonlinearities can be observed. This is the case for  $^{27}\text{Al}$  under stationary DNP conditions. To the nonlinear line intensities of Fig. 11, a Boltzmann distribution can be fitted which then leads to the quoted spin temperatures of  $\pm 5$  mK for a ruby crystal with  $\vartheta=60.4^\circ$ ,  $\theta_L=1.6$  K, and  $B_0=1.14$  T. Similarly, the spin temperature of  $^{17}\text{O}$  was measured to either  $\pm 5$  mK for a sample under similar conditions.

### III. NMR LASER DYNAMICS

In this section we examine the dynamic behavior of the solid-state NMR laser, both experimentally and theoretically. In contrast to the coherent radiation sources in the optical and microwave range, the output of the ruby NMR laser is strongly influenced by the energy-transfer characteristics of the coupled spin systems, particularly in the Q-

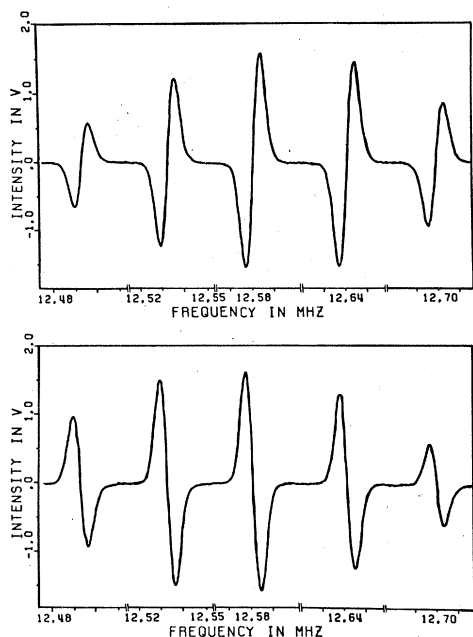


FIG. 11.  $^{27}\text{Al}$  NMR signals of the five  $\Delta m = \pm 1$  transitions with  $B_0 = 1.1$  T,  $\theta_L = 1.6$  K, and  $\vartheta = 60.4^\circ$ . The relative signal intensities correspond to a spin temperature of +5 mK in the upper and -5 mK in the lower picture.

switched p mode. Hence, the results of Sec. II are essential not only for a qualitative understanding of the NMR laser dynamics but for a quantitative description as well.

Again, we base our considerations on the heat-reservoir model. The dense  $^{27}\text{Al}$  Zeeman reservoir of Sec. IIA, however, is divided up into five (in general different) subsystems of fictitious spin- $\frac{1}{2}$  particles. In a quasiequilibrium state, each subsystem can be characterized by its own temperature and heat capacity. These reservoirs  $\{\mathcal{H}_{\text{Al},k}\}$  correspond to the five  $\Delta m = \pm 1$  NMR transitions of the  $I = \frac{5}{2}$   $^{27}\text{Al}$  nuclei which, due to electric quadrupole effects, have different NMR frequencies  $\omega_k$ .

#### A. NMR-laser-active spins

We have shown in Sec. IIC 4, that a negative nuclear-spin temperature of some millikelvin can be obtained in  $\text{Al}_2\text{O}_3:\text{Cr}^{3+}$  if a microwave pump heats the electronic dipole-dipole reservoir  $\{\mathcal{H}_{\text{ss}}\}$ , which causes negative DNP by thermal contact. The populations of the nuclear-spin states are thus inverted, and the nuclear magnetization is opposite to the static field.

Now, we tune the coil of the LC circuit to the

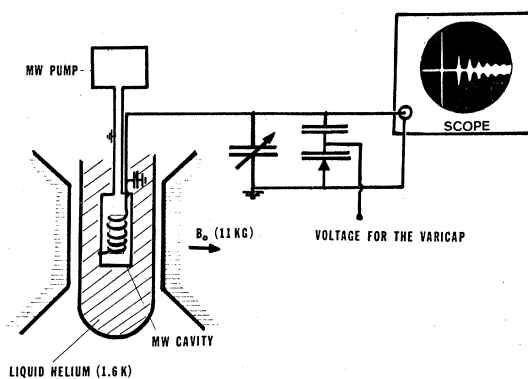


FIG. 12. Schematic diagram of the experimental setup for the detection of the NMR laser signals.

NMR frequency  $\omega_k$  of one of the  $^{27}\text{Al}$  subsystems. A transverse rotating magnetization  $M_{vk}$  may appear spontaneously, inducing an rf voltage which can be observed directly on the oscilloscope as indicated in Fig. 12.

A single-mode operation with  $\omega_r \cong \omega_k$  is possible if the longitudinal magnetization  $M_{zk}$ , of only that subsystem  $k$  to which the coil is tuned, is pumped below the critical threshold value  $M_{zk}^{\text{th}} < 0$ . The superradiant system with spins performing the coherent oscillation is then called the NMR-laser active reservoir  $\{\mathcal{H}_{\text{Al},r}\}$ . The remaining subsystems with  $\omega_j \neq \omega_k$  can be lumped together into the NMR-laser-inactive reservoir  $\{\mathcal{H}_{\text{Al},0}\}$ . Its spins flip incoherently only. However, the stored spin energy of  $\{\mathcal{H}_{\text{Al},0}\}$  can flow by thermal contact via  $\{\mathcal{H}_{\text{ss}}\}$  to  $\{\mathcal{H}_{\text{Al},r}\}$  as depicted in the energy flow diagram.

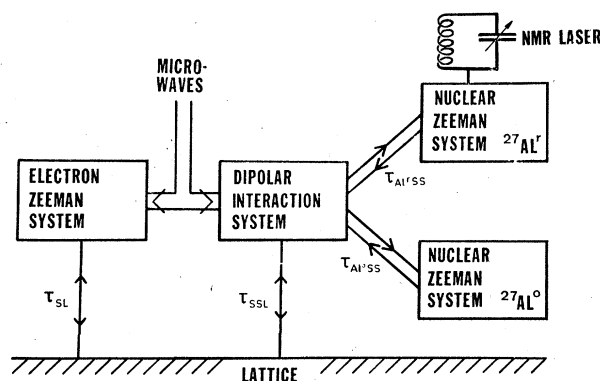


FIG. 13. Modified energy-flow diagram for the ruby NMR laser: The nuclear  $^{27}\text{Al}$  reservoir is split into a NMR-laser active and a NMR-laser-interactive system  $\{\mathcal{H}_{\text{Al},r}\}$  and  $\{\mathcal{H}_{\text{Al},0}\}$ , respectively. The energy transfer between the nuclear Zeeman reservoirs stems from the coupling to the electronic dipolar interaction system.

for the single-mode NMR laser in Fig. 13.

Multimode operations are also possible if the respective longitudinal magnetizations of more than one  $^{27}\text{Al}$  Zeeman subsystem are pumped below their (in general different) threshold values.

Since we restrict our present considerations principally to the single-mode NMR laser, the subscript  $k$  is dropped. Henceforth,  $M_z$ ,  $M_v$ , and  $M_z^{\text{th}}$  describe the NMR-laser-active spins.

### B. Single-mode NMR laser states

Within the framework of a phenomenological theory, the single-mode NMR laser can be described by three macroscopic variables  $M_z$ ,  $M_v$ , and  $B_1$ , respectively. As remarked above,  $M_z$  and  $M_v$  are the longitudinal and transverse component of the magnetization of  $^{27}\text{Al}^r$ , and  $B_1$  is the rotating component of the rf field inside the coil.

We set

$$B_1 = B_1^{\text{ind}} + F_B(t),$$

where  $B_1^{\text{ind}}$  is due to the induced voltage of  $M_v$ , and  $F_B(t)$  is the resonant fraction of the fluctuating field of the thermal noise current in the coil.

In accord with experimental facts, we assume that the precession frequency of  $M_v$  and therefore the NMR laser frequency  $\omega_r$  is equal to the cw NMR frequency  $\omega_k$ . This requires proper tuning such that  $\omega_c = 1/(LC)^{1/2}$  is equal to  $\omega_r$ . With this condition,  $M_v$  and  $B_1^{\text{ind}}$  are  $90^\circ$  out of phase, and the NMR laser operates in the absorption mode. If we further assume that the ringing time of the circuit  $T_c = 2Q/\omega_c$  is short with respect to all other time constants of the system (a condition which is always fulfilled) we have

$$|B_1^{\text{ind}}| = \frac{1}{2}\mu_0\eta Q M_v,$$

with  $\eta$  the filling factor and  $Q$  the quality factor of the coil.

Since the  $^{27}\text{Al}^r$  spins form a fictitious spin- $\frac{1}{2}$  system, variables  $M_z$ ,  $M_v$ , and  $B_1$  are transformed to fictitious variables  $M'_z$ ,  $M'_v$ , and  $B'_1$ . We then postulate that they obey Bloch-type equations which, in a frame of reference rotating with  $\omega_r$  about  $B_0$ , are

$$\begin{aligned} \frac{dM'_v}{dt} &= \gamma M'_z B'_1 - \frac{M'_v}{T_2}, \\ \frac{dM'_z}{dt} &= -\gamma M'_v B'_1 - \frac{1}{T_e} (M'_z - M'_e), \end{aligned} \quad (3.1)$$

$$B'_1 = -\frac{1}{2}\mu_0\eta Q M'_v + F_B(t).$$

Here  $T_2$  is the spin-dephasing time proportional to the inverse cw NMR linewidth of  $^{27}\text{Al}^r$ . The term  $(M'_z - M'_e)/T_e$  represents implicitly the pump and relaxation mechanisms. The effective magnetization  $M'_e$  to which  $M'_z$  relaxes, as well as the effective relaxation time  $T_e$  depend in a complicated way on the spin dynamics. They can be related to the time constants and to the inverse spin temperatures of the relevant spin-energy reservoirs of Sec. II, and to the microwave pump power. In general,  $M'_e$  is a complicated function of time determined by the solutions of Eqs. (2.3).

If  $\{\mathcal{H}_{A1}^r\}$  corresponds to the central  $(\frac{1}{2}, -\frac{1}{2})$  line, we obtain from matrix-element considerations  $M'_z = M_z$ ,  $M'_e = M_e$ ,  $M'_v = \frac{1}{2} M_v$ , and  $B'_1 = 3B_1$ . Thus, the true NMR laser variables fulfill the equations

$$\begin{aligned} B_1 &= -\frac{1}{2}\mu_0\eta Q M_v + F_B(t) \\ \frac{dM_v}{dt} &= 9\gamma M_z B_1 - \frac{1}{T_2} [M_v + F_{M_v}(t)], \\ \frac{dM_z}{dt} &= -\gamma M_v B_1 - \frac{1}{T_e} (M_z - M_e), \end{aligned} \quad (3.2)$$

with the initial condition  $M_z(0) = M_v(0) = M_{v0}$ .

#### 1. Steady-state oscillations and stability

As a limiting case, we consider a situation where  $T_e$  and  $M_e$  in Eqs. (3.2) have constant values, and where the fluctuations can be neglected. After eliminating the  $B_1$  field in (3.2), we obtain

$$\begin{aligned} \frac{dM_v}{dt} &= -\frac{9}{2}\mu_0\eta Q \gamma M_z M_v - \frac{M_v}{T_2}, \\ \frac{dM_z}{dt} &= \frac{1}{2}\mu_0\eta Q \gamma M_v^2 - \frac{M_z - M_e}{T_e}. \end{aligned} \quad (3.3)$$

Possible steady-state solutions are  $M_z^{\text{st}} = M_e$ , and  $M_v^{\text{st}} = 0$ . Evidently,  $M_z^{\text{st}}$  is stable. To investigate the stability of  $M_v^{\text{st}}$ , we set  $M_v^{\text{st}} = M_{v0} \exp(\Omega t)$  which, inserted in (3.3), leads to the condition

$$\Omega = -\frac{9}{2}\mu_0\eta Q \gamma M_e - 1/T_2.$$

Thus we can define the NMR laser threshold by

$$M_z^{\text{th}} = -2/9\mu_0\eta Q \gamma T_2 < 0, \quad (3.4)$$

and we find immediately that  $M_v^{\text{st}} = 0$  is stable if  $M_e \geq M_z^{\text{th}}$ . As we shall see more explicitly below,  $M_v^{\text{st}} = 0$  becomes unstable with an exponential growth of  $M_v$ , if the NMR laser is pumped below the threshold value  $M_z^{\text{th}}$ . A transition to a new steady state  $M_v^{\text{st}} \neq 0$  takes place where  $M_v$  plays the role of an order parameter. If  $M_e$  is close to the threshold, we can neglect the time derivative  $dM_z/dt$  in (3.3). Thus,  $M_z$  can be eliminated, and we end up with a single differential equation for  $M_v$  which has the typical form of a dynamic equa-

tion for an order parameter:

$$\frac{dM_v}{dt} = -\alpha M_v - \beta M_v^3 + F_B(t),$$

with

$$\alpha = \frac{1}{T_2} + \frac{9}{2} \mu_0 \eta Q \gamma M_e, \quad (3.5)$$

$$\beta = \frac{9}{4} \mu_0^2 \eta^2 Q^2 \gamma^2 T_e.$$

Neglecting again the fluctuations, we obtain the stable steady-state solution

$$M_v^{st} = \pm (-\alpha/\beta)^{1/2}. \quad (3.6)$$

The transition from  $M_v^{st} = 0$  to  $M_v^{st} = \pm (-\alpha/\beta)^{1/2}$ , if  $M_e < M_e^{th}$ , can be regarded as a disorder-order transition which resembles in many respects a second-order phase transition at thermal equilibrium. In the state  $M_v^{st} = 0$ , the  $^{27}\text{Al}^I$  spins flip incoherently due to spin-spin interactions. But the fluctuating rf field  $F_B(t)$  initiates an organized motion of the spins which, in turn, produce the slaving field  $B_1^{ind}$ . It can maintain a cw NMR laser oscillation.

To illustrate the analogy with a second-order phase transition more closely, we introduce the effective potential

$$\Phi = \frac{1}{2} \alpha M_v^2 + \frac{1}{4} \beta M_v^4, \quad (3.7)$$

from which the induced force terms at the rhs of (3.5) can be obtained by differentiation with respect to the order parameter and multiplication by  $-1$ . The potential is depicted in Fig. 14 for different values of  $\alpha$ . In going from  $\alpha < 0$  to  $\alpha > 0$ , the system passes through the critical point. For  $M_e = M_e^{th}$ , we have  $\Omega = 0$ . This then can be interpreted as a critical slowing down or soft mode.

Finally, from (3.6), we can calculate the steady-state order parameter

$$M_v^{st} = \frac{2}{3T_2 \eta Q \gamma \mu_0} \left[ \left( \frac{T_2}{T_e} \right) \frac{M_e - M_z^{th}}{M_z^{th}} \right]^{1/2} \quad (3.8)$$

The longitudinal component  $M_z^{th}$  and  $M_e$  can also be expressed in terms of the inverse spin temperature  $\beta_{Al}$  and  $\beta_{th}$ . In the high temperature limit we have

$$M_e = \frac{1}{Z} \frac{\hbar^2 \omega_k}{2k_B} N_0 \gamma \beta_{Al}, \quad M_z^{th} = \frac{1}{Z} \frac{\hbar^2 \omega_k}{2k_B} N_0 \gamma \beta_{th},$$

with  $Z$  the partition function,  $\omega_k$  the resonance frequency, and  $N_0$  the number of  $^{27}\text{Al}^I$  spins per unit volume. Thus for  $\beta_{Al} - \beta_{th} < 0$  we obtain

$$M_v^{st} = 3 M_z^{th} \left[ \left( \frac{T_2}{T_e} \right) \frac{\beta_{Al} - \beta_{th}}{\beta_{th}} \right]^{1/2}. \quad (3.9)$$

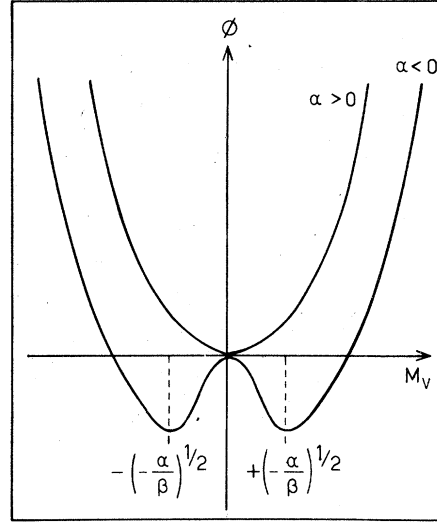


FIG. 14. The effective potential  $\phi = \frac{1}{2} \alpha M_v^2 + \frac{1}{4} \beta M_v^4$  for  $\alpha > 0$  and  $\alpha < 0$ , respectively.

The cw output in function of the pumping power, as given in our letter,<sup>1</sup> is compatible with (3.8) and (3.9).

To compare the threshold condition with experimental facts, it is convenient to introduce the so called radiation damping time  $T_R$ . For the central  $(\frac{1}{2}, -\frac{1}{2})$  line, in particular, we set

$$T_R = 2/9 \mu_0 \eta Q \gamma |M_z|. \quad (3.10)$$

Thus, in accord with (3.4), the threshold can also be characterized by

$$T_R^{th} = 2/9 \mu_0 \eta Q \gamma |M_z^{th}|, \quad (3.11)$$

or in other words, the system can perform a superradiant transition with  $M_v \neq 0$ , if  $T_R < T_2$ . Similar expressions with different numerical factors can be introduced, if one wants to test the threshold of the satellite lines.

TABLE II. Longitudinal magnetization  $M_0 = M_{z,\min}$  and calculated radiation damping time  $T_R$  for different  $Q$  values in comparison to the dephasing time  $T_2$  for all five NMR transitions with  $B_0 = 1.1$  T,  $\psi = 60.4^\circ$ ,  $\eta = 0.575$ ,  $\theta_L = 1.6$  K, and  $\theta_{Al} = -6$  mK.

Transition	$M_0$ (A/m)	$T_2$ ( $\mu\text{sec}$ )	$T_R$ ( $\mu\text{sec}$ )		
			$Q = 60$	$Q = 80$	$Q = 200$
$(-\frac{5}{2}, -\frac{3}{2})$	-3.47	27.2	38.5	28.9	11.5
$(-\frac{3}{2}, -\frac{1}{2})$	-3.12	28.8	26.8	20.1	8.0
$(-\frac{1}{2}, +\frac{1}{2})$	-2.80	30.6	26.5	19.9	8.0
$(+\frac{1}{2}, +\frac{3}{2})$	-2.53	27.2	33.2	24.9	10.0
$(+\frac{3}{2}, +\frac{5}{2})$	-2.28	27.2	58.8	44.1	17.6

In Table II we give explicit results for the most negative polarization  $M_0 = M_{z, \min}$  obtained with our system, for the dephasing time  $T_2$  found from cw line widths, and for the calculated radiation damping time  $T_R$  for coils of various  $Q$  and the filling factor  $\eta = 0.575$ . Experimentally, these results are confirmed. Only those modes with  $T_R < T_2$  could actually be excited.

## 2. NMR laser transients

If the ruby NMR laser is pumped far beyond threshold and subsequently tuned with the electrically controlled  $Q$  switch, a delayed pulse pattern is the result. Again, we consider the  $(\frac{1}{2}, -\frac{1}{2})$  transition and base the quantitative analysis of the transient signal on the NMR laser equations (3.2). However, the pump and relaxation term  $(M_z - M_e)/T_e$  has to be cast into a form which explicitly makes use of the results of Sec. II. Furthermore, the fluctuations  $F_B(t)$  must be related to the Nyquist noise of the  $LC$  circuit.

Since the variation of  $M_z$  and  $M_e$  are small within a time interval  $T_2$ , it is reasonable to express  $M_z$  as a function of the population numbers of the NMR-laser-active Zeeman states and, hence, as a function of the inverse spin temperature of the corresponding heat reservoir. Similarly,  $M_e$  is expressed in terms of the inverse temperatures of the electronic dipole-dipole system. Analytically,  $M_z$  and  $M_e$  can thus be derived from Eqs. (2.4).

The effective mean-square noise voltage of the coil with the resistance  $R$ , which induces NMR transitions within the linewidth  $\Delta\omega_k$ , is  $\overline{V_n^2} = (2/\pi) k_B \theta_n R \Delta\omega_k$  with  $\theta_n$  the noise temperature of the circuit. This noise voltage then induces a fluctuating transverse magnetization

$$\overline{M_{vn}^2} = (9 M_z \gamma T_2)^2 \frac{k_B \Theta_n Q \Delta\omega_k}{\mu_0 \omega_k 2\pi^2 \gamma^2 l},$$

with  $\omega_k$  the NMR frequency, and  $l$  and  $r$  the length

TABLE III. List of time constants for the NMR laser dynamics of the  $(\frac{1}{2}, -\frac{1}{2})$  transition with  $B_0 = 1.1 T$ ,  $\vartheta = 60.4^\circ$ ,  $Q = 60$ ,  $\theta_L = 1.6 K$ , and  $\theta_{Al} = -6$  mK.

$T_C = 1$	$\times 10^{-6}$ sec	Damping time of the $LC$ -circuit
$T_2 = 3$	$\times 10^{-5}$ sec	Coherence time of the spins in the disordered state
$T_R = 2.6$	$\times 10^{-5}$ sec	Radiation damping time of the NMR-laser-active system
$\tau_D \sim 2$	$\times 10^{-3}$ sec	Delay time of the first NMR laser pulse
$\tau_{Al^{0SS}} = 0.8$	sec	Coupling time constants
$\tau_{Al^r SS} = 0.2$	sec	
$\tau_{pol Al} = 60$	sec	Polarization time
$\tau_{dep Al} = 240$	sec	Relaxation time

and the radius of the coil, respectively. In order to incorporate the fluctuations into the NMR laser equations, we postulate that the spin-spin interactions tend to relax  $M_v$  towards  $M_{ve} = (\overline{M_{vn}^2})^{1/2}$ , rather than towards zero as it is usually assumed.

Thus by putting the various terms together, we obtain the following differential equations which replace Eqs. (3.3):

$$\begin{aligned} \frac{dM_v}{dt} &= -\frac{9}{2} \mu_0 \gamma \eta Q M_z M_v - \frac{1}{T_2} (M_v - M_{ve}), \\ \frac{dM_z}{dt} &= \frac{1}{2} \mu_0 \gamma \eta Q M_v^2 - \frac{6AC}{(6-15A\beta_{Al}^r)^2} \frac{1}{\tau_{Al^r SS}} (\beta_{Al}^r - \beta_{SS}), \\ \beta_{Al}^r &= 6M_z/AC + 15A M_z, \\ \frac{d\beta_{Al}^0}{dt} &= -\frac{1}{\tau_{Al^0 SS}} (\beta_{Al}^0 - \beta_{SS}), \\ \frac{d\beta_{SS}}{dt} &= -\frac{c_{Al}^0}{c_{SS}} \frac{1}{\tau_{Al^0 SS}} (\beta_{SS} - \beta_{Al}^0) \\ &\quad - \frac{c_{Al}^r}{c_{SS}} \frac{1}{\tau_{Al^r SS}} (\beta_{SS} - \beta_{Al}^r) - \frac{1}{\tau_{SSL}} (\beta_{SS} - \beta_L) \\ &\quad + \pi (\gamma_S B_1^{MW})^2 g(\omega_S - \omega_m) \frac{\omega_S - \omega_m}{\delta \omega^2} \\ &\quad \times [\omega_S \beta_S - (\omega_S - \omega_m) \beta_{SS}], \end{aligned} \quad (3.12)$$

$$\beta_S = \beta_L, \quad A = \hbar \omega_k / k_B, \quad C = N_0 \gamma \hbar / 2 \mu_0.$$

Since a pronounced hierarchy of time constants exists in our sample, as indicated in Table III, the nonlinear dynamic equations can be solved with appropriate approximations in distinct time regimes.

For short times after the tuning pulse to the  $Q$  switch ( $T_C, T_R, T_2 \ll t \ll \tau_{Al^r SS}, \tau_{Al^0 SS}$ ), the solution has the shape of a single delayed burst. The characteristic delay time  $\tau_D$  reflects the size of the transverse spin fluctuations  $M_{ve}$  induced by the Nyquist noise of the coil. In Fig. 15, the experimental envelope of the delayed pulse is confronted with the solutions of Eqs. (3.3) with the parameters  $B_0 = 1.1 T$ ,  $\omega_k = 2\pi \times 12.20$  MHz,  $Q = 60$ ,  $\eta = 0.575$ ,  $\vartheta = 60.4^\circ$ ,  $\Theta_{Al} = 1/k_B \beta_{Al} = -6$  mK, and  $M_{ve} \sim 10^{-7}$  A/m. The peak power amounts to 8 mW.

For intermediate times ( $\tau_{Al^r SS}, \tau_{Al^0 SS} \ll t \ll \tau_{pol}, \tau_{dep}$ ), the influence of the microwave pump as well as the spin-lattice relaxation can still be neglected. The transient signal is the same whether or not the microwaves are turned off after the  $Q$ -switch procedure. In this particular time regime the coupling of  $\{\mathcal{H}_{Al^0}\}$  and  $\{\mathcal{H}_{Al^r}\}$  to  $\{\mathcal{H}_{SS}\}$  becomes the decisive factor in determining the envelope of the superradiant oscillations. Retaining in Eqs. (3.12) the relevant terms only, the computer reproduces, indeed, the observed pulse se-

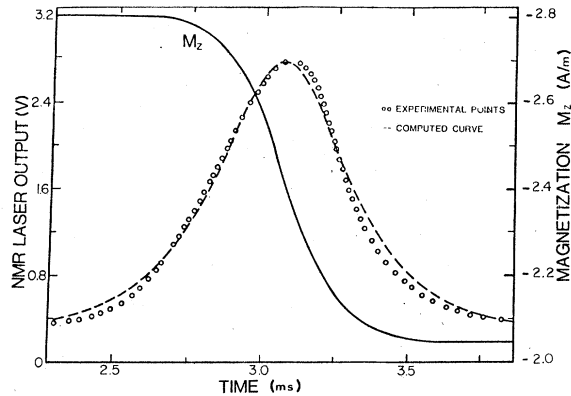


FIG. 15. Experimental (circles) and computed (dashed-line) NMR laser output voltage and computed  $z$  component  $M_z$  (solid line) of the magnetization for the first superradiant pulse (short-time regime) after tuning to the  $(\frac{1}{2}, -\frac{1}{2})$  transition.

quence which finally evolves into a quasistationary spin oscillation. There,  $\{\mathcal{H}_{A1^0}\}$  and  $\{\mathcal{H}_{A1^r}\}$  reach a common spin temperature. Figure 16 shows the experimental signal together with the computed envelope ( $\sim M_v$ ) and the time evolution of the longitudinal magnetization  $M_z$ . Both numerical solutions,  $M_v$  and  $M_z$ , were obtained from Eqs. (3.12) using the same sample parameters as above and fitting the time elapsed between the first and second pulse with the time constants  $\tau_{A1^0 SS} = 0.2$  sec and  $\tau_{A1^r SS} = 0.8$  sec of Table III.

Finally, in the long-time regime, where spin energy is continually radiated away, the level of the NMR laser oscillation either decreases to a lower value or decays to zero depending on the power of the microwave pump. For a large enough input the ultimate steady-state level of the rf radiation is determined by Eq. (3.8).

In view of the simplicity of the Bloch-type approach, the agreement between theory and experiment is satisfactory. Especially the result of Fig. 16 can be considered as the direct proof of the existence of the electron dipole-dipole reservoir and demonstrates the strong influence of  $\{\mathcal{H}_{SS}\}$  on the spin dynamics in ruby. However, some questions remain open. In particular, we have no definite proof yet that the NMR laser signal is purely absorptive, as is assumed. A dispersive contribution<sup>23</sup> can not be ruled out unless the phase of the rotating component and of the magnetization with respect to  $B_1^{\text{ind}}$  and its frequency can be measured with high enough precision.

### C. Multimode NMR laser states

We found further that the NMR laser can be operated also at several of the different NMR fre-

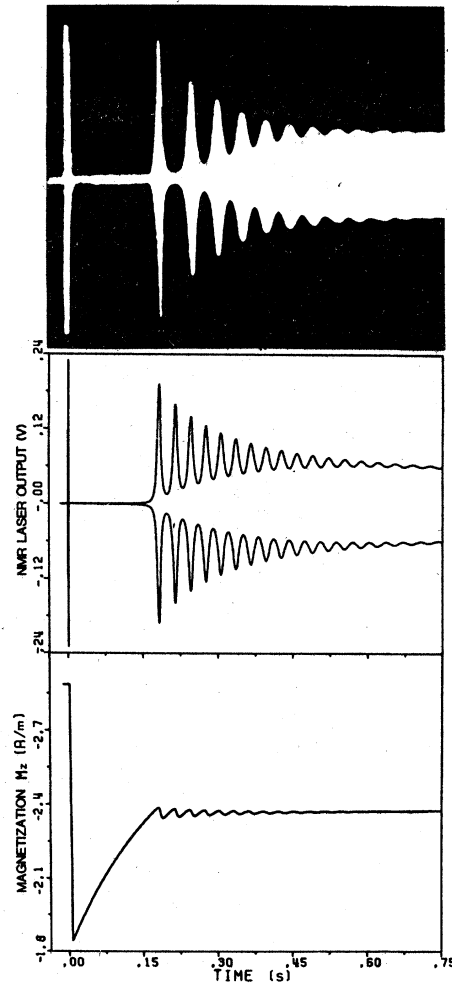


FIG. 16. Experimental pulse pattern together with the corresponding computer solution of Eqs. (3.12) for  $M_v$  ( $M_v \sim V$ ) and  $M_z$  for the  $(\frac{1}{2}, -\frac{1}{2})$  transition for intermediate times. The first pulse of  $M_v$  is clipped; its true intensity is shown in Fig. 15.

quencies of the quadrupolar split lines. Here, more than one  $^{27}\text{Al}$  Zeeman subsystem becomes NMR laser active, either sequentially or simultaneously. This is the case, if the  $Q$  is improved which amounts to an increase of the threshold value  $M_z^{\text{th}}$ . With such a system we produced NMR laser pulses of 400 V peak-to-peak and a corresponding power of about 25 W. In the cw mode, beats were observed from which the anticipated difference frequencies could be determined.

In the p mode, the most striking phenomenon is the appearance of a delayed multipulse transient after  $Q$ -switch tuning, as shown in Fig. 17. In the short-time regime, with  $Q = 150$  and the  $LC$  circuit tuned to the central  $(\frac{1}{2}, -\frac{1}{2})$  transition while keeping the other parameters given in Sec. II B 2

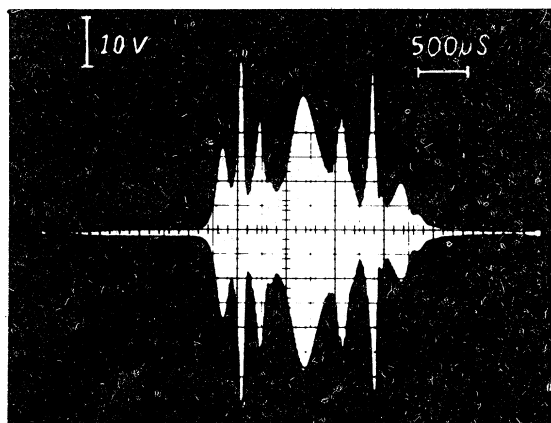


FIG. 17. NMR laser response in the short-time regime with a higher  $Q$  value. Instead of one superradiant burst as in Fig. 15, a pulse sequence is observed corresponding to various  $\Delta m = \pm 1$  NMR transitions of  $^{27}\text{Al}$ .

constant, seven pronounced peaks can be seen which correspond consecutively to the  $(\frac{1}{2}, -\frac{1}{2})$ ,  $(-\frac{1}{2}, -\frac{3}{2})$ ,  $(\frac{1}{2}, -\frac{1}{2})$ ,  $(\frac{3}{2}, \frac{1}{2} | -\frac{3}{2}, -\frac{5}{2})$ ,  $(\frac{1}{2}, -\frac{1}{2})$ ,  $(-\frac{1}{2}, -\frac{3}{2})$ , and  $(\frac{1}{2}, -\frac{1}{2})$  NMR transitions. Preliminary results of this sort can qualitatively be understood with an extended set of the Bloch-type equations (3.12). However, many features of such pulse pattern call for a more refined theory.

#### IV. CONCLUDING REMARKS

The dynamic properties of the new solid-state nuclear-spin-flip ruby NMR laser which have been presented together with a discussion of the

conventional aspects of spin relaxation and DNP in this system can be understood with an appropriate set of Bloch-type equations. The spontaneous transition of a nuclear-spin system to a collective, superradiant state, where longitudinal Zeeman order is transformed to transverse spin order, finds a consistent explanation with regard to the threshold, the critical behavior near threshold, the ignition by fluctuations, and the transient pulsation far from the threshold, if only a single mode is excited. The quantitative description of the multimode excitation is more difficult, particularly if mode coupling exists. In this case a fast transfer of coherence is anticipated which may lead to complicated interference effects, requiring a density-matrix approach, presumably.

Finally, we remark that such a NMR laser should be extremely sensitive to a change of its parameters and to externally applied perturbations such as pressure, electric fields, ultrasound, etc. Since similar properties are expected to be found in other systems, a wide variety of new experiments can be foreseen. We hope to report on some of these possibilities elsewhere.

#### ACKNOWLEDGMENTS

We wish to thank Dr. Courtens, IMB Rüslikon, Switzerland, for his stimulating help with regard to the role of the Nyquist noise. This paper was based on a dissertation submitted to the University of Zurich by one of us (P.B.) in partial fulfillment of the requirements for the Ph. D. degree. This work was supported in part by the Swiss National Science Foundation (Schweizerischer Nationalfond).

<sup>1</sup>P. Bösiger, E. Brun, and D. Meier, *Phys. Rev. Lett.* **38**, 602 (1977).

<sup>2</sup>P. Bösiger, E. Brun, and D. Meier, *Sixth International Symposium on Magnetic Resonance, Banff, Alberta Canada, 1977* (unpublished), p. 15.

<sup>3</sup>L. D. Landau, C. R., *Dokl. Akad. Nauk SSSR* **44**, 311 (1944).

<sup>4</sup>E. Hopf, *Ber. Verh. Saechs. Akad. Wiss. Leipzig Math.-Phys. Kl.* **94**, 1 (1942).

<sup>5</sup>H. Haken, *Synergetics* (Springer-Verlag, Berlin, 1977).

<sup>6</sup>See, e.g., Ch. Normand, Y. Pomeau, and M. G. Velarde, *Rev. Mod. Phys.* **49**, No. 3, 581 (1977).

<sup>7</sup>L. L. Butshvili, *Sov. Phys. JETP* **22**, 1277 (1966).

<sup>8</sup>M. A. Kozhushner, *Sov. Phys. JETP* **29**, 136 (1969).

<sup>9</sup>W. T. Wenckebach, T. J. B. Swanenburg, and N. J. Poulis, *Phys. Rep.* **14**, 181 (1974).

<sup>10</sup>V. A. Atsarkin, A. E. Mefed, and M. I. Rodak, *Sov. Phys. JETP* **28**, 877 (1969).

<sup>11</sup>E. E. Hundt, Thesis (University of Zurich, 1972) (unpublished).

<sup>12</sup>E. E. Hundt, H. H. Niebuhr, B. Derighetti, and E. Brun, *Proceedings of the Sixteenth Congress Ampere, 1971*

(unpublished), p. 953.

<sup>13</sup>Ch. Gabathuler, Thesis (University of Zurich, 1974) (unpublished).

<sup>14</sup>Ch. Gabathuler, E. E. Hundt, and E. Brun, *Proceedings of the Seventeenth Congress Ampere, Turku, Finland* (North-Holland, Amsterdam, 1973), p. 499.

<sup>15</sup>M. Goldman, S. F. J. Cox, and V. Bouffard, *J. Phys. C* **7**, 2940 (1974).

<sup>16</sup>W. de Boer, T. O. Niinikoski, *Nucl. Instrum. Methods* **114**, 495 (1974).

<sup>17</sup>M. Goldman, *Spin Temperature and NMR in Solids* (Clarendon, Oxford, 1970).

<sup>18</sup>O. S. Leifson, E. Vogel, *Phys. Rev. B* **2**, 4626 (1970).

<sup>19</sup>V. Petricek, M. Odehnal, *Nucl. Instrum. Methods* **52**, 197 (1967).

<sup>20</sup>G. R. Khutsishvili, in Ref. 14, p. 35.

<sup>21</sup>P. Bösiger, Thesis (University of Zurich, 1977) (unpublished).

<sup>22</sup>N. Laurance, E. C. McIrvine, and J. Lambe, *J. Phys. Chem. Solids* **23**, 515 (1962).

<sup>23</sup>A. Redfield (private communication).

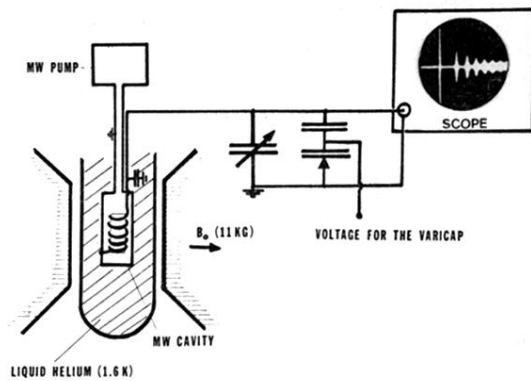


FIG. 12. Schematic diagram of the experimental setup for the detection of the NMR laser signals.

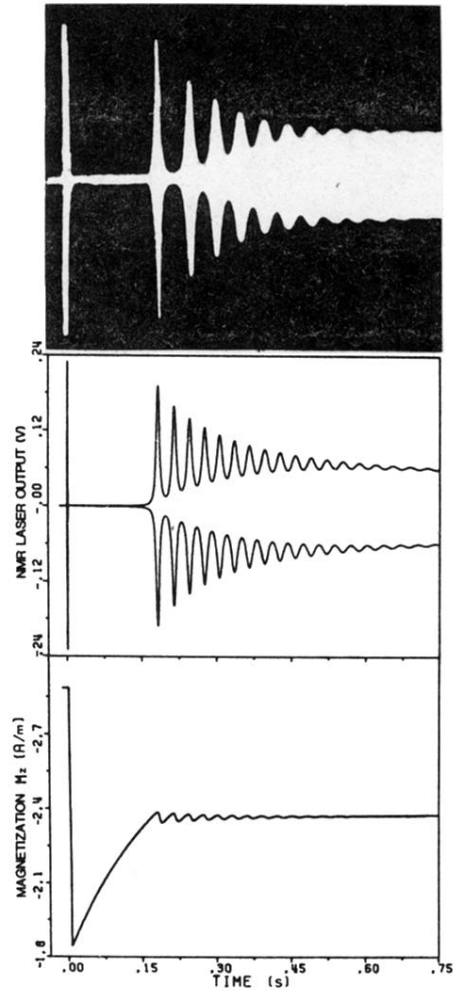


FIG. 16. Experimental pulse pattern together with the corresponding computer solution of Eqs. (3.12) for  $M_v$  ( $M_v \sim V$ ) and  $M_z$  for the  $(\frac{1}{2}, -\frac{1}{2})$  transition for intermediate times. The first pulse of  $M_v$  is clipped; its true intensity is shown in Fig. 15.

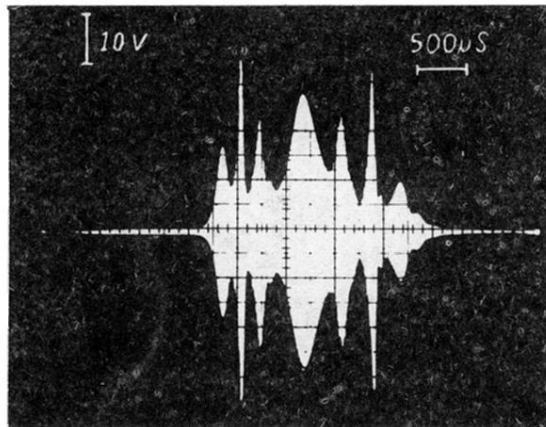


FIG. 17. NMR laser response in the short-time regime with a higher  $Q$  value. Instead of one superradiant burst as in Fig. 15, a pulse sequence is observed corresponding to various  $\Delta m = \pm 1$  NMR transitions of  $^{27}\text{Al}$ .